PAPER • **OPEN ACCESS**

Study of the Electron cyclotron power deposition in TOMAS

To cite this article: J Buermans *et al* 2024 *Phys. Scr.* **99** 085606

Physica Scripta

PAPER

Study of the Electron cyclotron power deposition in TOMAS

J Buermans[1,2], A Adriaens[1,2], S Brezinsek[3], K Crombé[1,2], L Dittrich[4], A Goriaev[1], Yu Kovtun[5], L D López-Rodríguez[1,2], P Petersson[4] and M Van Schoor[1]

[1] Laboratory for Plasma Physics, LPP-ERM/KMS, Brussels, Belgium
[2] Department of Applied Physics, Ghent University, Ghent, Belgium
[3] Institute for Energy and Climate Research, Forschungszentrum Jülich GmbH, Jülich, Germany
[4] Fusion Plasma Physics, KTH Royal Institute of Technology, Stockholm, Sweden
[5] Institute of Plasma Physics, NSC KIPT, Kharkov, Ukraine

E-mail: Johan.Buermans@ugent.be

Keywords: plasma, fusion, TOMAS, breakdown, experiments, Electron cyclotron resonance heating

OPEN ACCESS

RECEIVED
4 March 2024

REVISED
17 June 2024

ACCEPTED FOR PUBLICATION
3 July 2024

PUBLISHED
12 July 2024

Abstract

Efficient Electron Cyclotron Resonance Heating (ECRH) breakdown and pre-ionization can be achieved with fundamental X-mode, while higher harmonics can introduce excessive stray radiation. Fundamental heating however is characterized by a low cut-off density, introducing additional power absorption mechanisms in the plasma. A good knowledge of these mechanisms is necessary to use fundamental X-mode as an efficient pre-ionization method. Numerous experiments were performed on the TOroidally MAgnetized System (TOMAS) to study the power deposition for ECRH in helium. It is a facility designed to study plasma production, wall conditioning and plasma-surface interactions and is operated by LPP-ERM/KMS at the FZ-Jülich. The influence of the injected power P_{EC} and the magnetic field B_0 on the absorption mechanisms is examined, in order to reduce stray radiation and improve the absorption efficiency. This will allow to determine the best scenarios for plasma start-up and pre-ionization.

1. Introduction

In view of ITER First Plasma operation, experiments and modeling are performed to describe breakdown and plasma initiation [1–3]. Assisting the plasma startup by Electron Cyclotron Resonance Heating (ECRH) is recommended [4–6] and sometimes found to be necessary [7] in larger devices. Simulations predict that at least 4 MW of ECRH assist would be required in ITER [1].

Efficient ECRH breakdown and pre-ionization can be achieved with fundamental X-mode [8]. It is however characterized by a low cut-off density, introducing additional power absorption mechanisms in the plasma [9]. Higher harmonic heating is generally used to overcome this density barrier [7]. The absorption efficiency is however strongly reduced [9, 10], introducing excessive stray radiation in the vessel which can damage the wall or diagnostics [11, 12].

A good knowledge of the ECRH absorption mechanisms beyond this cut-off density is necessary to use fundamental X-mode as an efficient pre-ionization method. Numerous experiments were performed on the TOroidally MAgnetized System (TOMAS) to study the power deposition for ECRH in helium, with the aim to determine the absorption mechanisms for several conditions, to improve the absorption efficiency and therefore reduce the stray radiation.

We will start with a description of the TOMAS device and the experimental setup, followed by an overview of the performed experiments. Second we will characterize the ECRH power source to determine the injected power. Then we will determine the fraction of reflected power for several values of the injected power P_{EC}, the magnetic field B_0 and the gas pressure. Also the influence of the Langmuir probe position and the wave polarization on the reflected power is examined. This will allow us to determine the amount of power coupled to the plasma.

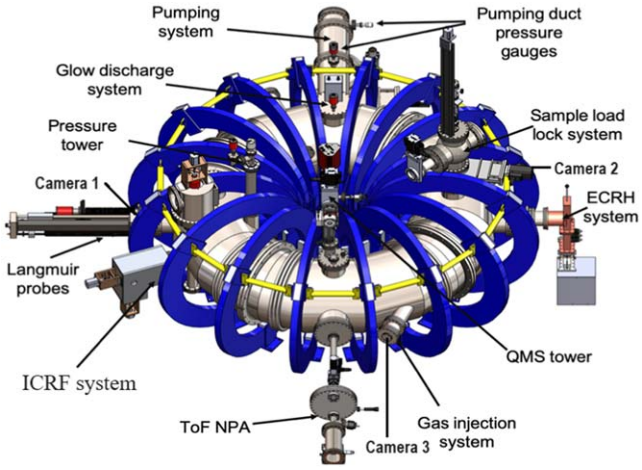

Figure 1. The TOMAS device with several plasma production systems and diagnostics.

Finally, the temperature and density profiles, obtained by a triple Langmuir probe, will be used to determine the power deposition mechanisms present in the vessel. The influence of the injected power P_{EC} and the magnetic field B_0 will be examined. This will allow to determine the best scenarios for plasma start-up and pre-ionization.

2. The TOMAS device

The TOroidally MAgnetized System (TOMAS) [13, 14] (figure 1) is a facility designed to study wall conditioning, plasma—surface interactions and plasma production. It is operated by LPP-ERM/KMS at the FZ-Jülich. The metallic vessel has a plasma volume of 1.1 m^3, a major radius R = 0.78 m and a minor radius a = 0.26 m. The variable toroidal magnetic field can reach a maximum value of 125 mT on the torus axis, which equals a coil current of 2.2 kA. It is created by 16 copper coils. Several systems for plasma production are present: Glow Discharge (GD) system, Electron Cyclotron Resonance Heating (ECRH) system and Ion Cyclotron Range-of-Frequencies (ICRF) system.

Various plasma diagnostics are available [15]. The Langmuir probe system consists of two triple movable probes and one single probe. The optical diagnostics include a photo-detector, video diagnostics and optical emission spectroscopy. Particle diagnostics include a residual field energy analyzer, a residual gas analyzer (quadrupole mass spectrometer), a time-of-flight neutral particle analyzer and vacuum gauges.

3. Experimental setup

A first measurement in a helium plasma is performed, with a magnetic field $B_0 = 91.2\ mT$ (1600 A), RF power $P = 1200\ W$ with X-mode polarization and a pressure of $6.35 \cdot 10^{-4}\ mbar$ (He gas flow=70 sccm). The pulse has a length of 2 seconds and begins 0.5 s after the start of the data acquisition. The forwarded and reflected power are measured and obtained by the Data Acquisition system (DAQ) [14].

The electron density and temperature are readily obtained by triple Langmuir probe (TLP) measurements [15, 16]. Figure 2 shows the evolution of the forwarded and reflected power. Figure 3 shows the electron density and temperature evolution at the Electron Cyclotron Resonance (ECR) layer as measured by the TLP. A more or less steady state regime is observed between 1.18 s and 2.48 s.

The TLP is initially positioned at the Low Field Side (LFS) wall. It is then moved into the vessel where every 0.5 cm a plasma shot is performed (figure 4).

This way a radial scan of the electron density and temperature as a function of time is obtained (figure 5).

Reproducible conditions are achieved during a series af shots. These electron density and temperature measurements can be used to identify different absorption mechanisms in the plasma [9].

This procedure is repeated along the vertical direction in the center of the vessel. This way a horizontal (Figure 6) and vertical (figure 7) electron density and temperature profile can be obtained.

The experiments were performed in helium for different values of the power level (P_{EC}), the current in the magnetic field coils (I), the pressure (p) and the polarization of the injected wave (Pol). An overview is given in tables 1 to 3.

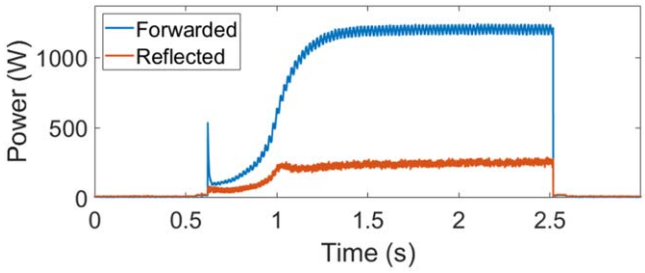

Figure 2. Evolution of the forwarded and reflected power as function of time for a nominal value of $P = 1200\ W$.

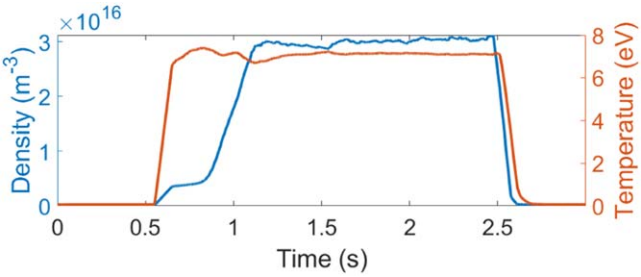

Figure 3. Electron density and temperature evolution at the ECR (+3.28 cm) for $B_0 = 91.2\ mT$ (1600 A), $P = 1200\ W$ and a pressure of $6.35 \cdot 10^{-4}\ mbar$.

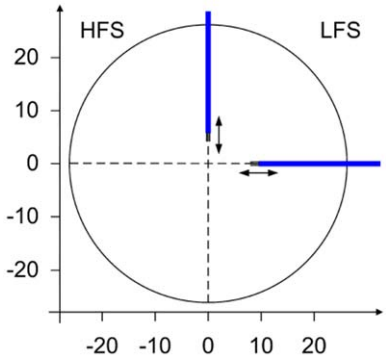

Figure 4. Position of the movable triple Langmuir probes on TOMAS.

4. The electron cyclotron source

The electron cyclotron source is a MUEGGE MH6000-213BF magnetron, which generates 2.45 GHz 0.6 kW—6 kW continuous wave (cw) output power (figure 8) [14]. A 3-stub tuner and an adjustable short are used for matching. A zero-bias Schottky diode measures the reflected power level.

A mode-converter is introduced in the 100 mm DN100 pipe to create the desired orientation of the injected wave. It consists of a metallic fin which can be orientated horizontally (O-mode) or vertically (X-mode). It can be removed to obtain an unpolarized wave (U-wave).

Microwaves transmitted into the vessel are partially absorbed by ECR. Changing the magnetic field allows us to shift the resonance layer along the diameter of the vessel in the toroidal plane. Partial absorption causes multiple reflections of the microwave in the vessel. It leads to multi-pass absorption and a microwave propagation and polarization mixture [9, 17].

4.1. Forwarded power

The power of the EC source is controlled by an input voltage which can vary between 0V and 10V. The nominal output power is theoretically comprised between 600W and 6000W. Several experiments were performed to verify the relation between the input voltage and the measured forwarded power.

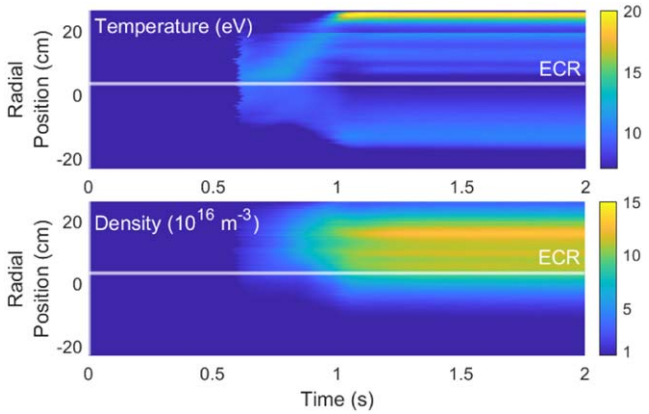

Figure 5. Electron density and temperature profile evolution in time for a radial scan in helium with $B_0 = 91.2\ mT$ (1600 A), $P = 1200\ W$ and a pressure of $6.35 \cdot 10^{-4}\ mbar$.

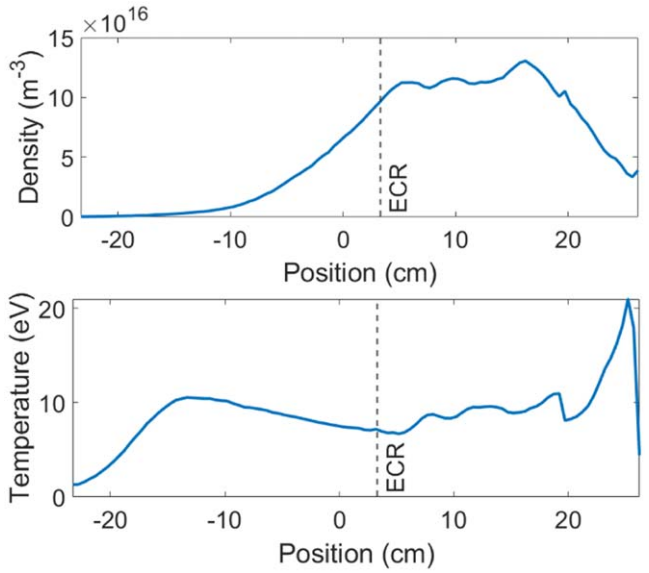

Figure 6. Horizontal density and temperature profiles obtained by the TLP for $B_0 = 91.2\ mT$ (1600 A), $P = 1200\ W$ and a pressure of $6.35 \cdot 10^{-4}\ mbar$ in helium (at $t = 2\ s$).

The results are presented in figure 9, which clearly confirms a linear relation. There is a very good agreement between the nominal value of the power and the experimental value for input voltages starting at 1.33V (800W). For lower values, the deviation becomes significant.

The nominal power however is not reached instantaneously, it rises gradually to its maximum value. The general shape of the forwarded power is depicted in figure 10 in red. It is clear that there is a 50 Hz ripple present in the measured signal.

Density and temperature measurements show that this 50 Hz ripple is also present in the plasma. We can conclude that this ripple is not introduced in the power measuring circuit but that it is introduced by the EC source itself. We can filter this ripple out of the data to reach a smooth evolution of the power (in blue).

The general shape of the forwarded power is characterized by several stages:

1. [$0.00 - 0.55\ s$] - No power is introduced into the vessel. The forwarded power measurements show a mean offset of 5.18 W in this time frame.
2. [$0.55 - 0.62\ s$] - There is a small ramp-up of the power up to a mean value of 17.01 W.

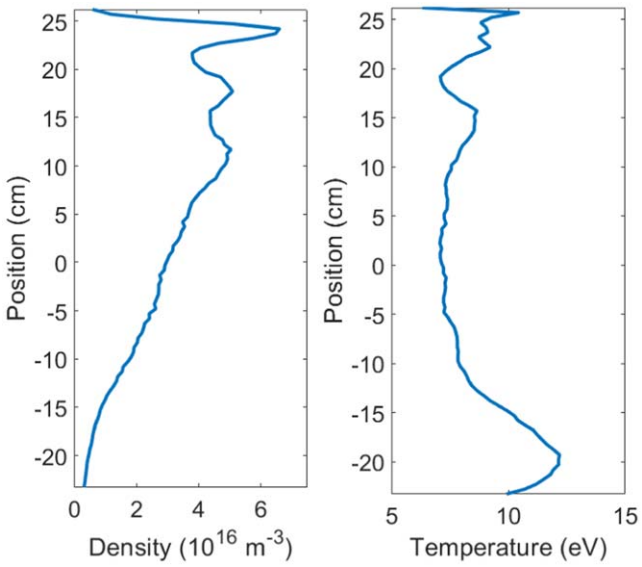

Figure 7. Vertical density and temperature profiles obtained by the TLP for $B_0 = 91.2\ mT$ (1600 A), $P = 1200\ W$ and a pressure of $6.35 \cdot 10^{-4}\ mbar$ in helium (at $t = 2\ s$).

Table 1. Helium - $6.3 \cdot 10^{-4}$ *mbar* - X-wave.

$p(mbar)$	Pol	$P_{EC}(W)$	$I(A)$
$6.3 \cdot 10^{-4}$	X	1200	1400
$6.3 \cdot 10^{-4}$	X	1200	1450
$6.3 \cdot 10^{-4}$	X	1200	1500
$6.3 \cdot 10^{-4}$	X	1200	1532
$6.3 \cdot 10^{-4}$	X	1200	1550
$6.3 \cdot 10^{-4}$	X	1200	1600
$6.3 \cdot 10^{-4}$	X	1200	1650
$6.3 \cdot 10^{-4}$	X	1200	1700
$6.3 \cdot 10^{-4}$	X	1200	1750
$6.3 \cdot 10^{-4}$	X	1200	1800
$6.3 \cdot 10^{-4}$	X	1200	1850
$6.3 \cdot 10^{-4}$	X	1200	1900

$p(mbar)$	Pol	$P_{EC}(W)$	$I(A)$
$6.3 \cdot 10^{-4}$	X	900	1600
$6.3 \cdot 10^{-4}$	X	1000	1600
$6.3 \cdot 10^{-4}$	X	1200	1600
$6.3 \cdot 10^{-4}$	X	1500	1600
$6.3 \cdot 10^{-4}$	X	2000	1600
$6.3 \cdot 10^{-4}$	X	2500	1600
$6.3 \cdot 10^{-4}$	X	3000	1600
$6.3 \cdot 10^{-4}$	X	3600	1600
$6.3 \cdot 10^{-4}$	X	4200	1600
$6.3 \cdot 10^{-4}$	X	4800	1600
$6.3 \cdot 10^{-4}$	X	5400	1600
$6.3 \cdot 10^{-4}$	X	6000	1600

3. [0.62 − 0.64 *s*] - There is a peak in the forwarded power up to 538.15 *W* which reduces immediately to a value of around 100 *W*.
4. [0.64 − 1.00 *s*] - The power rises increasingly up to about 580 *W*, where the maximum slope is obtained.
5. [1.00 − 1.38 *s*] - The power increase diminishes until more than 98% of the nominal value is reached.
6. [1.38 − 2.52 *s*] - The power stays constant with a mean value of 1200 *W*, which is the nominal power.

Table 2. Helium - $5.0 \cdot 10^{-4}$ *mbar* - X-wave.

$p(mbar)$	*Pol*	$P_{EC}(W)$	$I(A)$
$5.0 \cdot 10^{-4}$	X	1200	1400
$5.0 \cdot 10^{-4}$	X	1200	1500
$5.0 \cdot 10^{-4}$	X	1200	1600
$5.0 \cdot 10^{-4}$	X	1200	1700
$5.0 \cdot 10^{-4}$	X	1200	1800
$5.0 \cdot 10^{-4}$	X	1200	1900

$p(mbar)$	*Pol*	$P_{EC}(W)$	$I(A)$
$5.0 \cdot 10^{-4}$	X	900	1600
$5.0 \cdot 10^{-4}$	X	1200	1600
$5.0 \cdot 10^{-4}$	X	1500	1600
$5.0 \cdot 10^{-4}$	X	2000	1600
$5.0 \cdot 10^{-4}$	X	2500	1600
$5.0 \cdot 10^{-4}$	X	3000	1600

Table 3. Helium - $6.3 \cdot 10^{-4}$ *mbar* - O-wave.

$p(mbar)$	*Pol*	$P_{EC}(W)$	$I(A)$
$6.3 \cdot 10^{-4}$	O	1200	1400
$6.3 \cdot 10^{-4}$	O	1200	1500
$6.3 \cdot 10^{-4}$	O	1200	1600
$6.3 \cdot 10^{-4}$	O	1200	1700
$6.3 \cdot 10^{-4}$	O	1200	1800
$6.3 \cdot 10^{-4}$	O	1200	1900

$p(mbar)$	*Pol*	$P_{EC}(W)$	$I(A)$
$6.3 \cdot 10^{-4}$	O	900	1600
$6.3 \cdot 10^{-4}$	O	1200	1600
$6.3 \cdot 10^{-4}$	O	1500	1600
$6.3 \cdot 10^{-4}$	O	2000	1600
$6.3 \cdot 10^{-4}$	O	2500	1600
$6.3 \cdot 10^{-4}$	O	3000	1600

7. [$2.52 - 2.58$ *s*] - The power decreases very sudden and stabilizes around 16.84 *W*.
8. [$2.58 - 3.00$ *s*] - No power is introduced into the vessel anymore. The forwarded power measurements show the initial offset value of 5.18 *W*.

4.2. Reproducibility

First, the timing is investigated, to verify the variation of the start and end time of the power injection. For every value of the nominal power, 100 shots were performed to study the reproducibility of the forwarded power. The results for a nominal power value of 1200 *W* are depicted in figure 11. All shots were performed in helium with a magnetic field of 91.2 *mT* (1600 *A*) and a pressure of 6.3×10^{-4} *mbar*.

It is observed that the initial peak around 0.63 seconds shifts slightly between a minimum value of 0.5911 seconds and a maximum of 0.6325 seconds, resulting in a maximum offset of 40 *ms* (figure 12 (left)). A similar behavior is observed at the end of the shot (2.4774 and 2.5182 seconds) (figure 12 (right)). There is however no correlation between the timing of the initial peak and the ramp down for one particular shot. The start and end seem to have a random timing. This initial power peak originates probably in the EC source itself, that wants to ramp up to the set nominal power, notices too high reflections and reduces the injected power instantly to keep the reflected power below a specific threshold. Further investigation is needed to confirm this.

Second, the influence of the value of the nominal power on the different stages is investigated. The overall picture is shown in figure 13 where the evolution of the measured forwarded power is given for 6 different values of the nominal power.

For the first three stages (figure 14), there seems to be no influence of the value of the nominal power. The mean offset of 5.18W is always present in the first stage. The small ramp-up of the power up to a mean value of

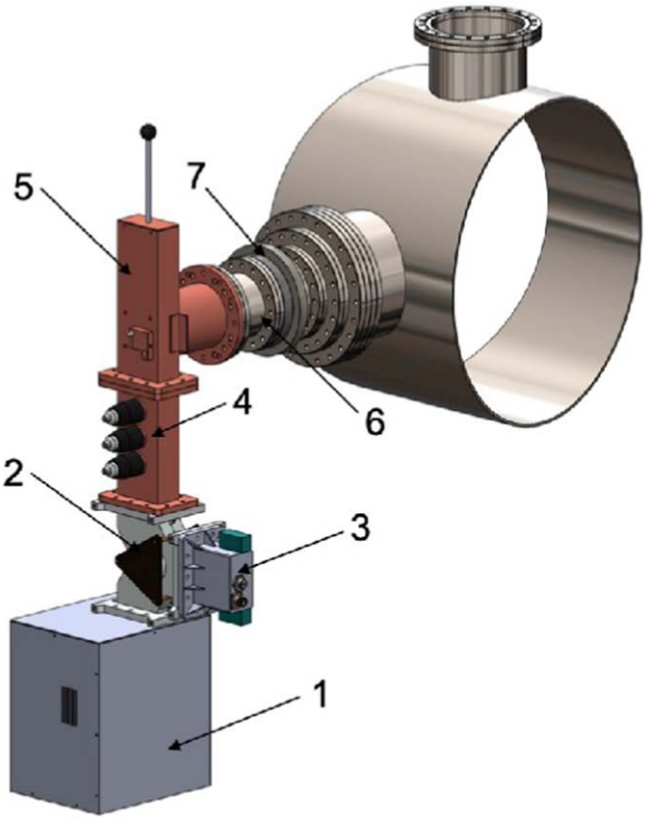

Figure 8. The TOMAS ECRH system:(1) MUEGGE MH6000-213BF magnetron, (2) Philips 2722 163 02 004 circulator, (3) Philips 2722 163 02 004 dummy load, (4) 3-stub tuner, (5) MUEGGE MW5002B-120YD transition element, (6) 100 mm DN100 pipe, and(7) fused silica UV window.

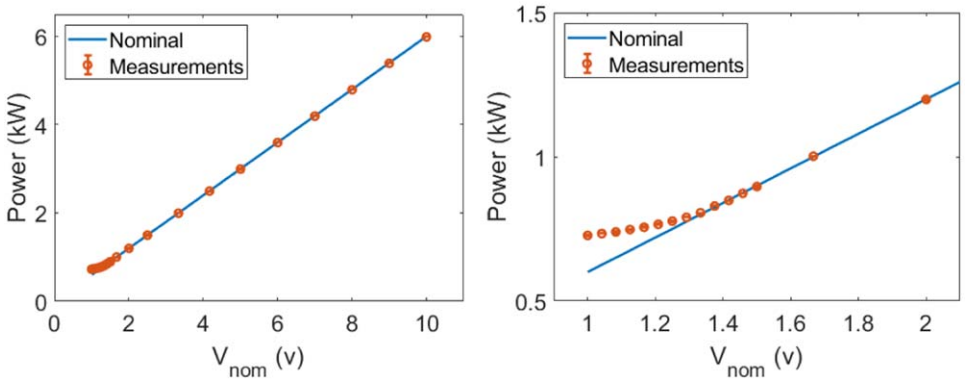

Figure 9. Comparison between the input voltage and the experimental (measured) forwarded power.

17.01W is always present in the second stage. The peak in the third stage has a mean value of $\approx 534W$ and there is no correlation between the value of the peak and the nominal power. The end of stage 3 is characterized by a value of $\approx 100W$. A similar random behavior of the start and end time is observed. There seems to be however a correlation between the start of stages 2 and 3.

Stages 4 and 5 are characterized by a ramp-up to 98% of the nominal value (figure 14). There seems to be no influence of the nominal power on the end of stage 5. The border between stages 4 and 5 however, where the maximum slope is obtained for a power of $\approx$50% of the nominal value, is influenced by the value of the nominal power. A higher value results in a shorter time interval for stage 4 and a steeper initial increase.

For stages 7 to 8, there doesn't seem to be any influence of the nominal power. The power stabilizes around 16.84W in stage 7 and reduces to the initial offset value of 5.18W. There is however a correlation between the

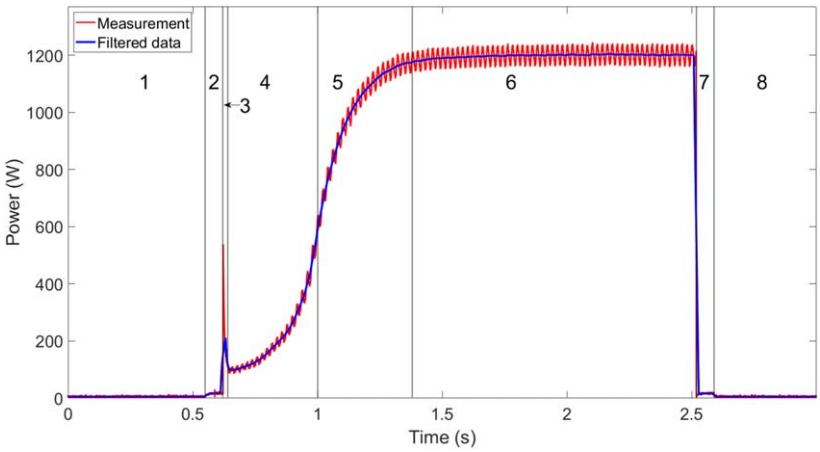

Figure 10. Different stages in the evolution of the forwarded power with a 50 *Hz* ripple (red) and the filtered signal (blue).

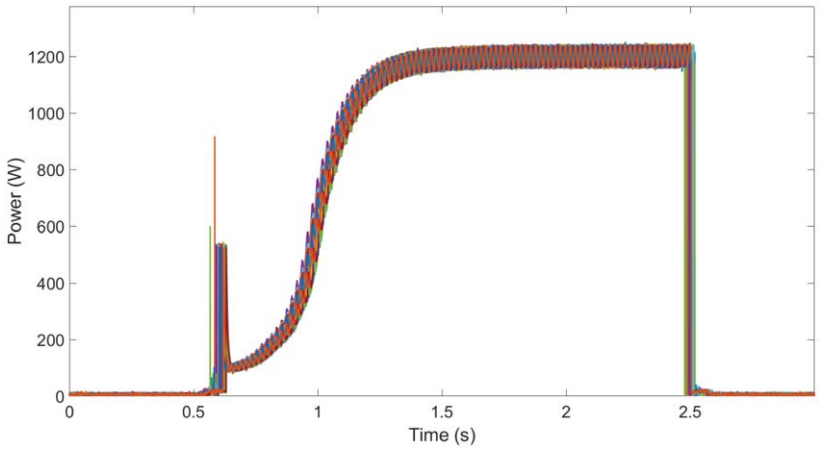

Figure 11. Measurements of the forwarded power for 100 consecutive shots with $P_{nom} = 1200\ W$.

start of stages 7 and 8. Finally, it was confirmed that there is no influence of the polarization of the injected wave, the pressure in the vessel, the magnetic field, the position of the Langmuir probe nor the used gas (hydrogen or helium) on the measurements of the forwarded power.

5. Power deposition

A first estimate of the amount of absorbed power can be obtained by looking at the difference between the injected power and the reflected power. Since the metallic vessel reflects almost completely the microwaves, the net absorbed power can be determined. To determine the location of the power absorption, we can also take a closer look at the temperature and density profiles. Density and temperature peaks are signs of resonant absorption or collisional damping.

5.1. Reflected Power

The reflected power is influenced by a lot of parameters:

- Power and polarization of the injected wave
- Absorption efficiency of the injected wave, determined by the plasma density and temperature
- Reflections and conversions
- The magnetic field strength, which influences in turn the plasma parameters

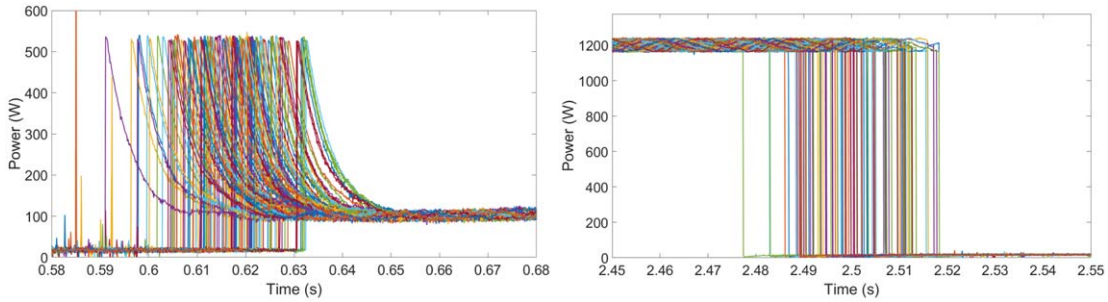

Figure 12. Power measurements for 100 consecutive shots with $P_{nom} = 1200\ W$: initial peak(left) and ramp down (right).

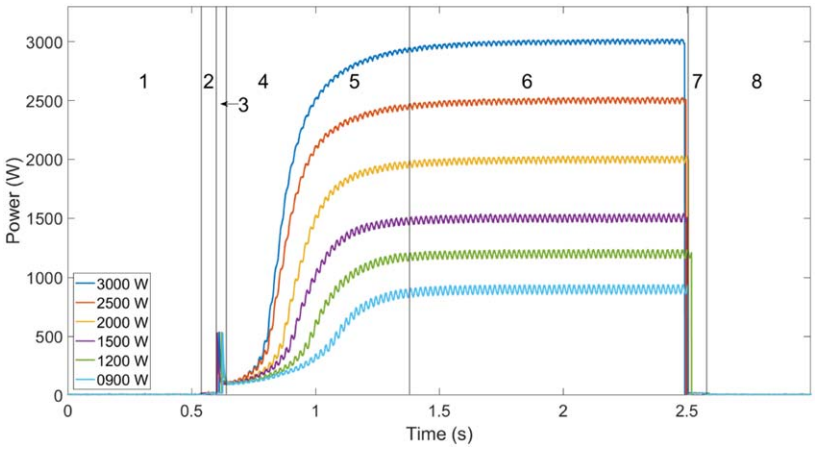

Figure 13. The influence of the nominal power on the different stages in the evolution of the forwarded power.

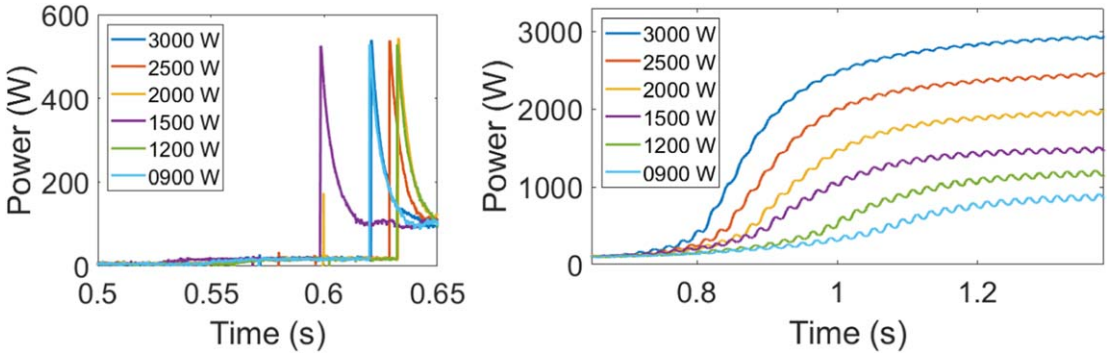

Figure 14. The influence of the nominal power on the forwarded power for stages 1-3 (left) and 4-5 (right).

However, if the same initial parameters are used—resulting in similar plasma parameters—there should be no difference observed in the reflected power, except for the influence of the Langmuir Probe. The probe itself can disturb the plasma, alter the plasma parameters and influence thereby the absorption efficiency.

5.1.1. Probe position

First, the influence of the position of the Langmuir probe on the reflection coefficient is investigated. This coefficient is determined as: $R = P_{refl}/P_{forw}$.

Figure 15 (top) shows R in function of time for different positions of the probe in the horizontal plane. All shots were performed in helium with a magnetic field of 91.2 mT (1600 A), 1200 W injected power (X-wave

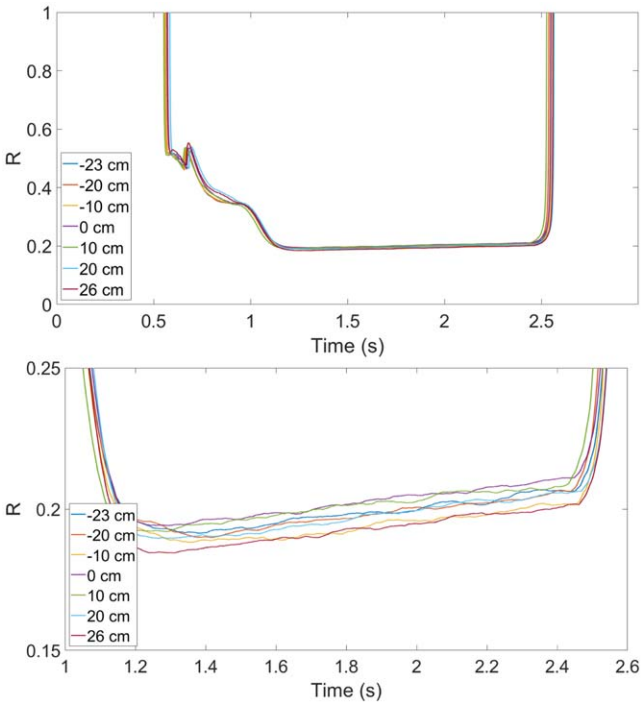

Figure 15. The influence of the horizontal TLP position on the reflection coefficient for a helium plasma with $B_0 = 91.2\ mT$ (1600 A), $P = 1200\ W$ X-mode polarization and a pressure of $6.35 \cdot 10^{-4}\ mbar$.

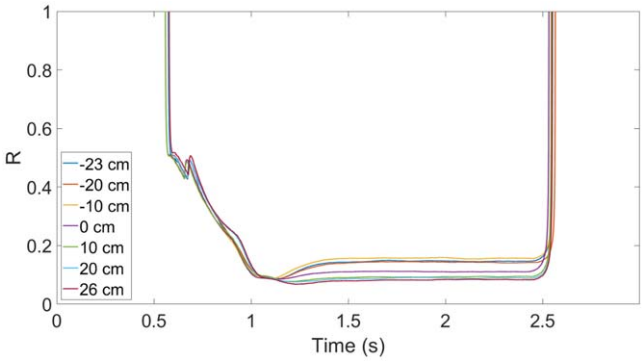

Figure 16. The influence of the horizontal TLP position on the reflection coefficient for a helium plasma with $B_0 = 91.2\ mT$ (1600 A), $P = 1200\ W$ O-mode polarization and a pressure of $6.35 \cdot 10^{-4}\ mbar$.

polarization) and a pressure of $6.3 \times 10^{-4}\ mbar$. It is clear that for these conditions the probe hardly influences the reflection coefficient.

A closer look at the data for several power levels confirms that sometimes a trend is visible for the influence of the probe position on the reflection coefficient: reflections increase when the probe is inserted more (figure 15 (bottom)). Sometimes this trend is not clearly present. The differences are however very small and could be influenced by small variations in the gas pressure.

We can conclude that the probe hardly influences the plasma for this specific value of the magnetic field ($B_0 = 91.2\ mT$). A closer look at the data for several magnetic fields, gas pressures or injected gasses, shows no significant influence of these factors on the reflected power. It just confirms the trend that inserting the probe deeper into the plasma increases only slightly the reflected power. A similar result is obtained for the vertical probe position.

A similar study was performed for O-wave polarization. The results are presented in figure 16. Here a similar trend is observed for most of the scans but the influence of the probe is more pronounced. The variation of the reflection coefficient is not negligible and rises up to more than 15%, depending on the magnetic field.

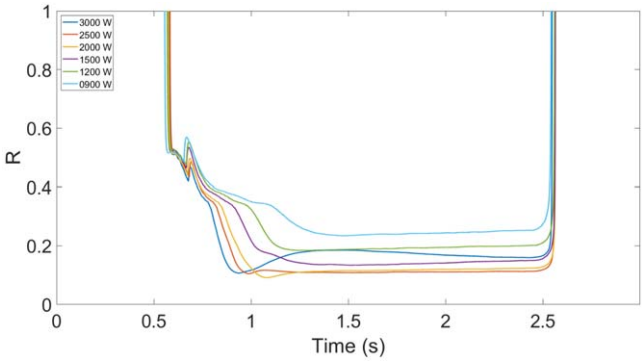

Figure 17. The influence of the nominal power on the reflection coefficient for a helium plasma with $B_0 = 91.2\ mT$ (1600 A), X-mode polarization and a pressure of $6.35 \cdot 10^{-4}\ mbar$.

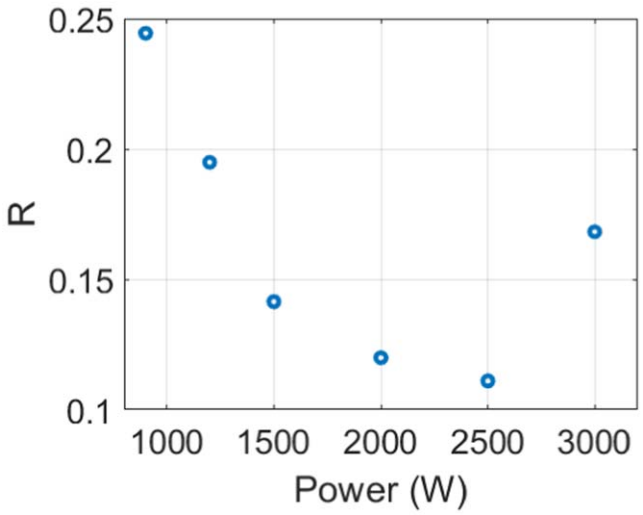

Figure 18. The influence of the nominal power on the reflection coefficient at $t = 2.0\ s$.

5.1.2. Power level

The injected power influences significantly the plasma production. The influence of the power on the reflection coefficient is investigated and shown in figure 17. All shots were performed in helium with a magnetic field of 91.2 mT (1600 A), a pressure of 6.3×10^{-4} $mbar$ and X-wave polarization. The probe was positioned at the wall to avoid any influence.

These traces show that in the initial phase of the plasma creation ($0.5\ s - 1.5\ s$) several regimes can be identified. The appearance of these regimes is influenced by the injected power level. After 1.5 seconds the plasma seems to be in stable regime. In this regime, we notice that with increasing power the reflection coefficient goes down up to a power level of 2500 W, afterwards the reflection rises a little (figure 18). There seems to be an optimal value for the injected power near 2500 W. A similar result is obtained for the vertical measurements.

5.1.3. Magnetic field

The magnetic field determines the position where the initial plasma is created. It is clear that this will influence the plasma parameters and hence the reflection coefficient. The results are presented in figure 19. All shots were performed in helium with a power of 1200 W X-wave polarization and a pressure of 6.3×10^{-4} $mbar$. The probe was positioned at the wall to avoid any influence.

It seems that the reflection coefficient rises exponentially for an increasing value of the magnetic field (figure 20). However the data for a magnetic field $B_0 = 96.9\ mT$ seems inconsistent with the other data. In

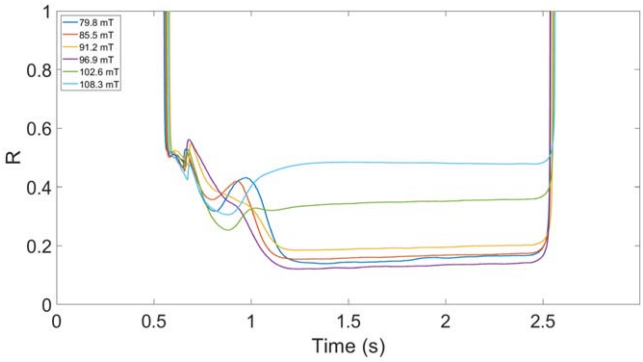

Figure 19. The influence of the magnetic field on the reflection coefficient for a helium plasma with $P = 1200\ W$, X-mode polarization and a pressure of $6.35 \cdot 10^{-4}\ mbar$.

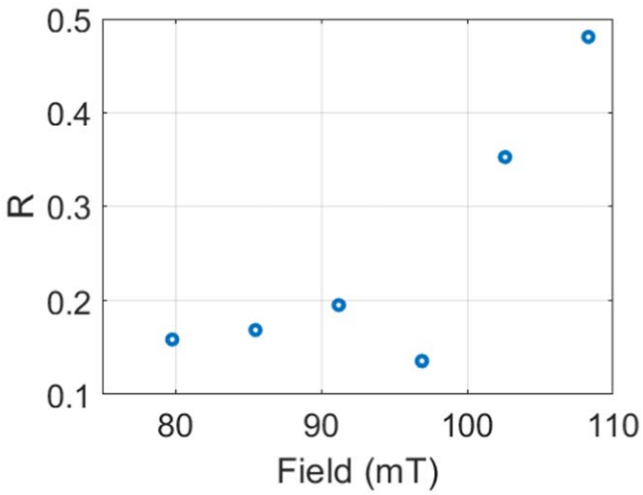

Figure 20. The influence of the magnetic field on the reflection coefficient at $t = 2.0\ s$.

general we can conclude that moving the resonance layer closer to the LFS increases the reflection coefficient. A similar result is obtained for the vertical measurements.

5.1.4. Wave polarization

The polarization of the injected wave determines the absorption mechanisms that occur in the plasma. The absorption efficiency of the different wave polarizations can be calculated based on the optical depth of EC waves [10]. We can conclude that O-wave absorption is to be 6 times lower than X-wave for TOMAS relevant temperatures and densities (figure 21). An influence on the reflection coefficient is thus expected.

Figure 22 shows this influence of the wave polarization on the reflection coefficient. It is clear that there are some differences for the two polarizations, but the effect is limited. The unpolarized wave seems to follow more or less the behavior of the X-wave. This can be explained by the fact that multiple reflections on the vessel wall causes polarization scrambling [18] which results in a mixture of polarizations present in the machine, independant from the orientation of the injected wave.

5.1.5. Gas pressure

When the gas pressure is lower, the reflection coefficient is generally higher, because less particles can interact with the injected wave.

However, the absorption efficiency doesn't depend solely on the number of particles as shown in figure 23. The initial evolution of the reflection coefficient seems to be similar in all cases (up to 1 *s*). An increasing pressure can lead to a higher reflection (red) or a significant reduction (blue) afterwards with respect to (nearly) vacuum

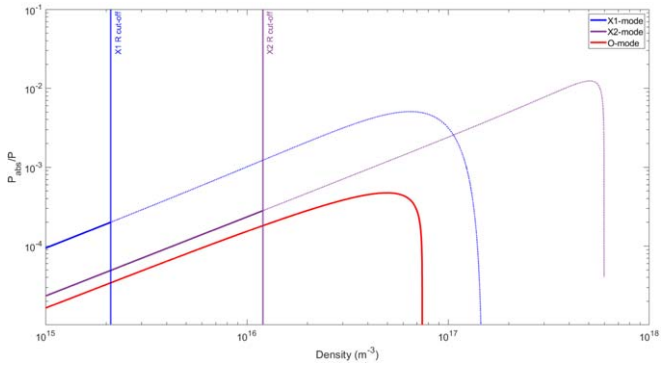

Figure 21. Absorption efficiency for different polarizations of the injected wave as function of the density ($T_e = 20\ eV$).

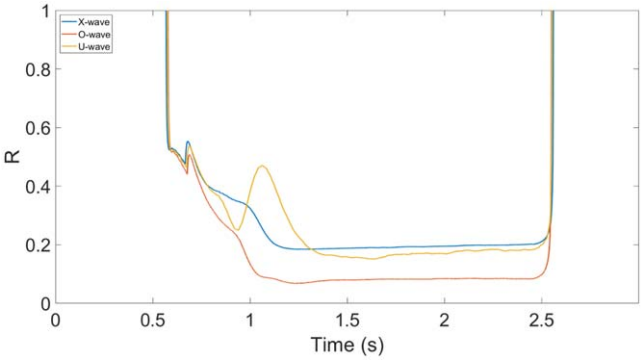

Figure 22. The influence of the polarization on the reflection coefficient for a helium plasma with $B_0 = 91.2\ mT$ (1600 A), $P = 1200\ W$ and a pressure of $6.35 \cdot 10^{-4}\ mbar$.

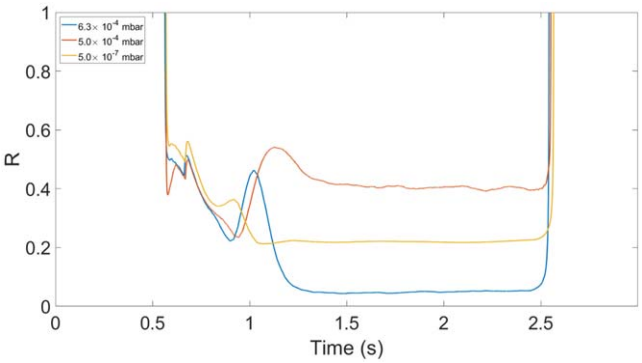

Figure 23. The influence of the pressure on the reflection coefficient for a helium plasma with $B_0 = 91.2\ mT$ (1600 A), $P = 1200\ W$ X-mode polarization.

conditions. It is clear that different absorption mechanisms occur here. The X-mode cut-off is exceeded in both high pressure cases ($6.3/5.0 \times 10^{-4}\ mbar$).

5.2. Power deposition profiles

Microwaves transmitted into the vessel are partially absorbed at the ECR layer. The low absorption efficiency requires multiple reflections on the walls and multipass absorption to create a plasma and raise the density [3, 9].

Due to reflections on the wall, the wave is depolarized and scattered, resulting in a mixture of O-mode and X-mode present in the vessel, independent of the polarization of the injected wave. This process is also called polarization scrambling [18]. Both O- and X-wave are consequently present in the machine and will lead to a

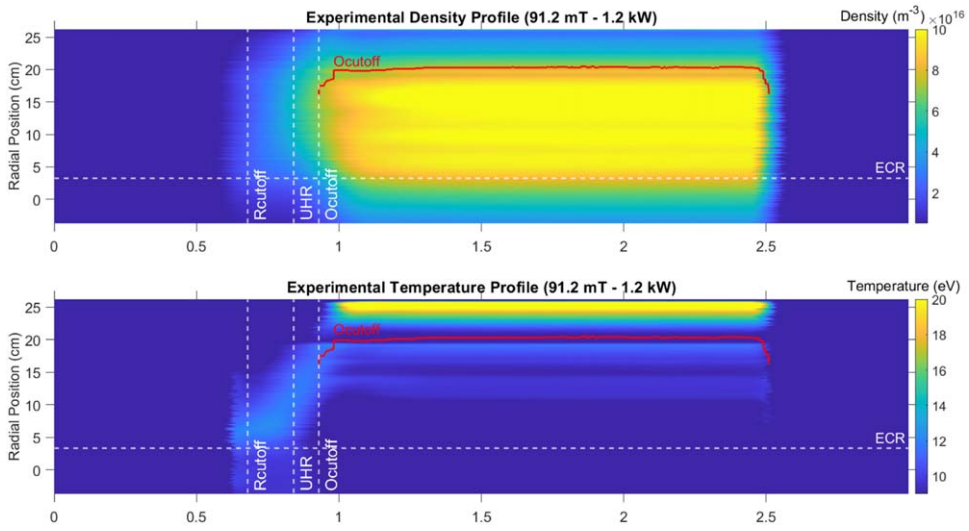

Figure 24. Electron density and temperature profile evolution for a helium plasma with $B_0 = 91.2\ mT$ (1600 A), $P = 1200\ W$ and a pressure of $6.35 \cdot 10^{-4}\ mbar$ in the central mid-plane.

multitude of heating regimes and power deposition mechanisms. These include Electron Cyclotron Resonance (ECR), Upper Hybrid Resonnance (UHR), mode conversion to the Electron Bernstein Wave (EBW) and collisional damping.

We can add the appearance of the R cut-off and the UHR (white dashed line) to the density and temperature profile evolution for a scan where a shot is taken every mm from the LFS, 30 cm into the plasma vessel (figure 24) with the standard pressure of $6.35 \cdot 10^{-4}\ mbar$. We can also add the appearance (white dashed line) and the evolution of the position of the O cut-off (red) as it appears at a fixed density $n_e = 7.45 \cdot 10^{16}\ m^{-3}$ (present between 0.93 and 2.51 s). The O cut-off has been used to calibrate the TLP [19]. These thresholds will help to identify the different power absorption mechanisms.

We can define 2 different regimes:

- **Plasma build-up:**including breakdown and a succession of different absorption mechanisms ($0.55 - 1.2\ s$).
- **Steady-state regime:** no change in the plasma parameters and deposition mechanisms ($1.2 - 2.5\ s$).

5.2.1. Plasma build-up

In the initial phase of the plasma production, mostly X-wave power deposition at the ECR layer will be responsible for the breakdown and density increase, as the absorption efficiency of the O-wave is 6 times lower [9]. Figure 25 shows that some additional peaks are visible near the ECR at +4.4 cm +6.3 cm for the temperature and the density. It also seems that the small peaks in the temperature profile seem to disappear. The erratic behavior of the profile with ups and downs becomes smoother from this point on.

When the R cut-off density is reached ($t = 0.68\ s$), only a part of the X-wave will tunnel trough the evanescent layer and couple at the ECR, where the density is raised (figure 26). Due to multiple reflections on the wall, this portion is increased. O-mode absorption is still 6 times lower and will hardly play a part.

The mean temperature stays quite constant around 10 eV. We can observe that the maximum temperature shifts to the LFS, following the position of the R cut-off (see figure 24). A small temperature bump is observed near +19 cm. Density is also raised more to the LFS. This can be explained by collisional damping of the tunneling wave in the evanescant zone.

The small density peaks near +4.4 cm +6.3 cm are still visible in the density profile. They correspond however with a slight decrease in temperature this time.

At $t = 0.84\ s$ the UHR appears and density rises even further (figure 27). We observe a density bump at ≈20 cm, while the temperature bump near +19 cm increases even further. We can observe that density near ≈16 cm is slightly elevated. At the HFS temperature drops slightly while the temperature near the LFS wall increases slowly. The density continues to rise until the O cut-off density is reached at $t = 0.95\ s$.

As density rises even further, both R cut-off and UHR will move to the LFS until a more or less stable regime is reached at about 1.2 s (figure 24). The O cut-off also moves slightly to the LFS. The temperature and density

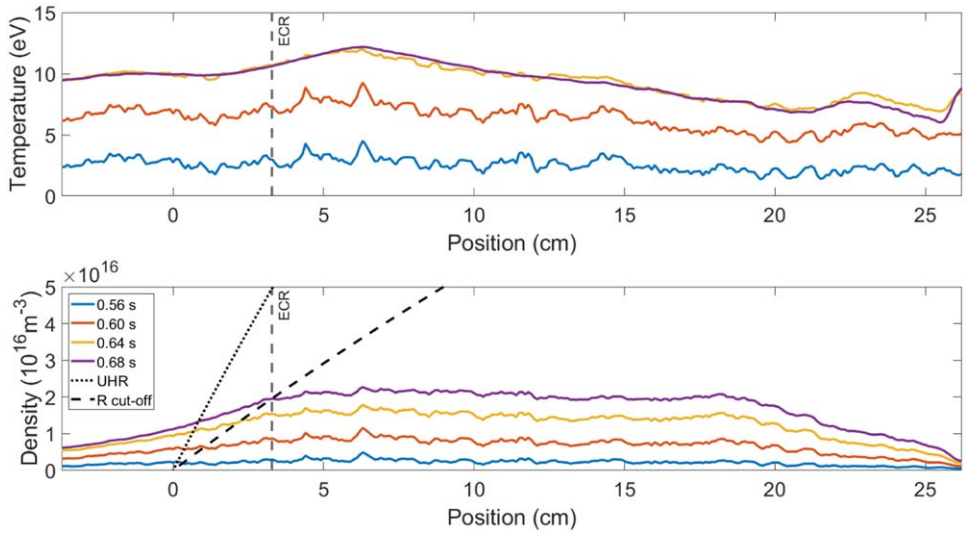

Figure 25. Evolution of the electron temperature and density profiles below the R cut-off density.

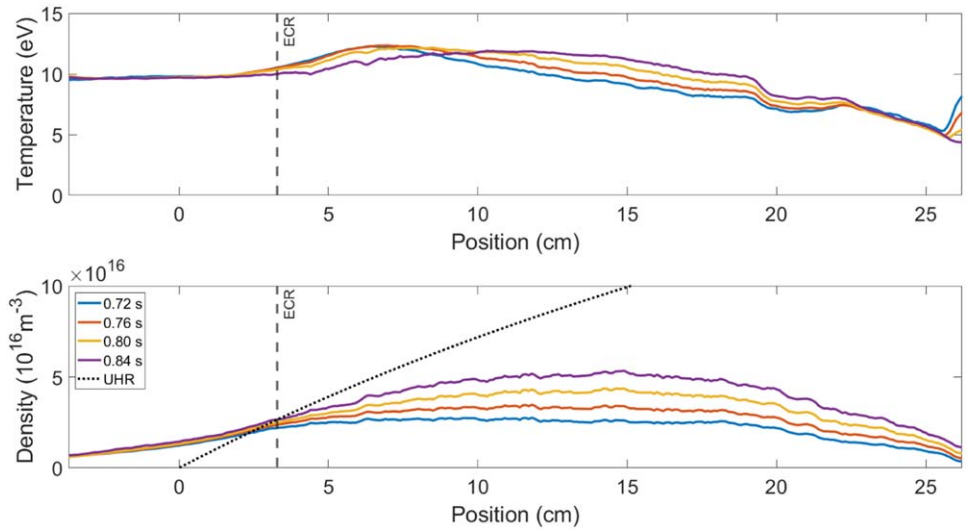

Figure 26. Evolution of the electron temperature and density profiles between the R cut-off and the UHR density.

profile evolution above the O cut-off is shown in figure 28. At the LFS wall, we notice that the temperature peaks quickly. At several locations between the ECR and the LFS we can also observe additional small temperature peaks.

We notice that the density rises slightly near ≈6 cm and ≈10 cm and continues to rise near ≈16 cm. It seems that this is linked to the appearance of the density bump near ≈20 cm .The cause of these additional peaks will be discussed in the next section.

At the HFS we notice a temperature peak which moves to the HFS, in a region where density is very low and no power deposition is expected (figure 5). In this region diffusion and convection probably counter each-other, which could cause turbulence and a rise in the temperature. This is beyond the scope of this article.

5.2.2. Steady-state regime

The steady state regime is characterized by a large temperature peak at the LFS wall, a region with raised temperature at the HFS (−13.3 cm) and additional temperature peaks in the temperature profile (figure 29).

The temperature raise at the HFS is probably caused by an interaction between diffusion and convection, which can cause turbulence and raise the temperature. This is beyond the scope of this article. A faint

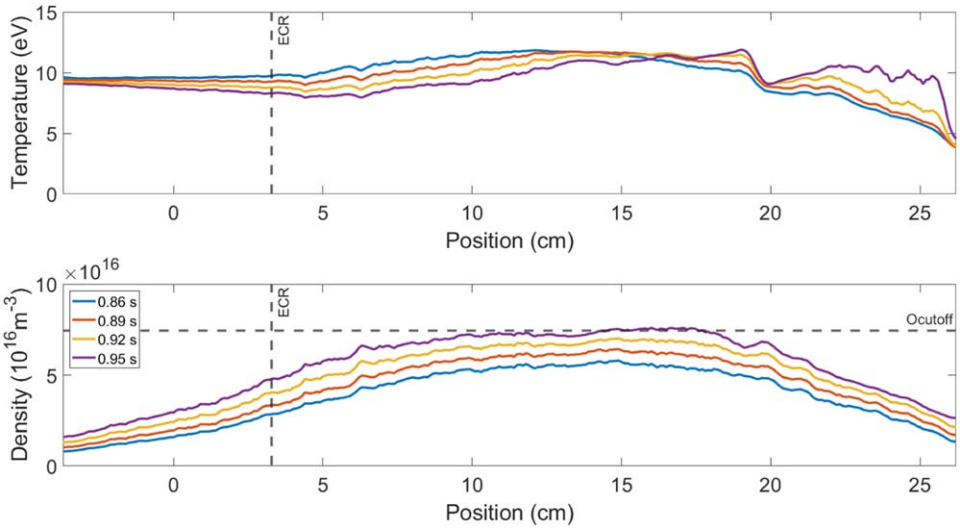

Figure 27. Evolution of the electron temperature and density profiles between the UHR and the O cut-off density.

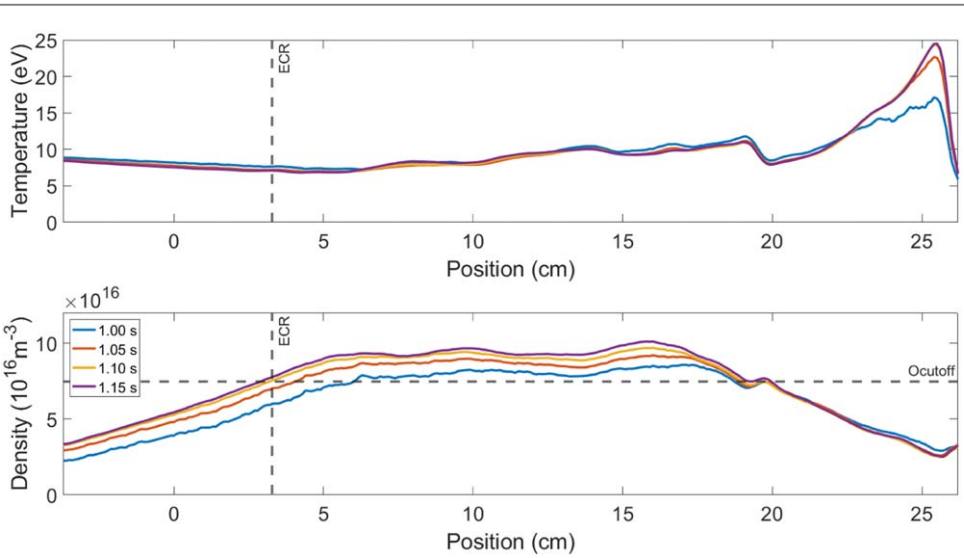

Figure 28. Evolution of the electron temperature and density profiles above the O cut-off density.

temperature peak is hardly visible at the ECR which could be caused by resonant absorption of the tunneling wave.

The large temperature peak at the LFS wall is probably due to plasma-wall interactions. Moving the resonance layer to the LFS, hence raising the plasma density at that location, increases the temperature peak (figure 30). Additionally, the injected X-waves are reflecting back and forth in the small region between the wall and the R cut-off and can loose energy through collisional damping. The temperature peak at 19.2 cm seems to be located near the O cut-off density. For the additional temperature peaks, we'll have to find another explanation.

The evanescent region for the X-wave is located at the LFS. Here we find close to each other the R cut-off and the UHR, where mode conversion to the Electron Bernstein Wave (EBW) is possible [20]. This mode conversion process is characterized by nonlinear phenomena of parametric instability, which can introduce for example Lower Hybrid Waves (LHW) in the plasma [21]. The non-monotonic density profile—as observed in figure 29 near the O cut-off at the LFS—can cause additional Parametric Decay Instabilities (PDI) [22–24]. This could be an explanation for the additional temperature peaks observed. This will have to be confirmed by dedicated experiments, for example by measuring the frequencies present in the vessel.

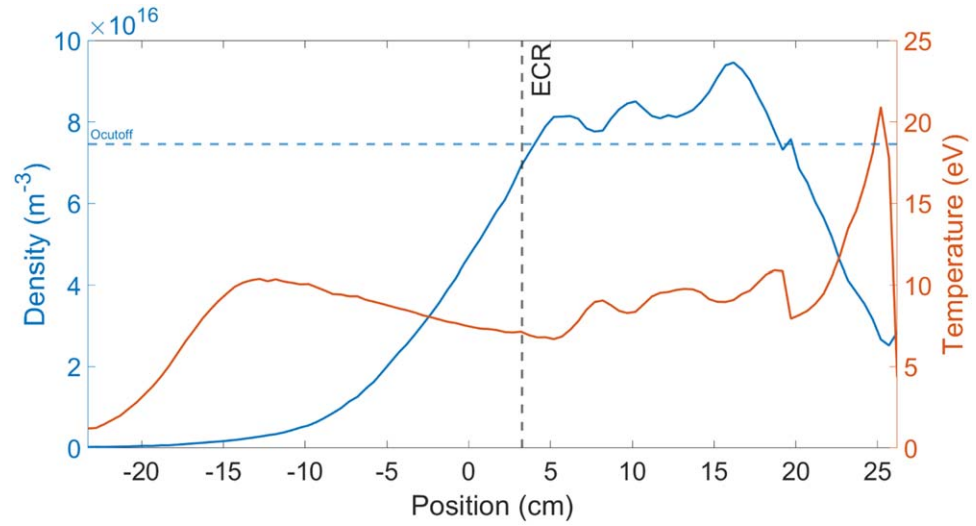

Figure 29. Electron density and temperature profile for a helium plasma with $B_0 = 91.2\ mT$ (1600 A), $P = 1200\ W$ X-mode polarization and a pressure of $6.35 \cdot 10^{-4}\ mbar$ at $t = 1.7\ s$.

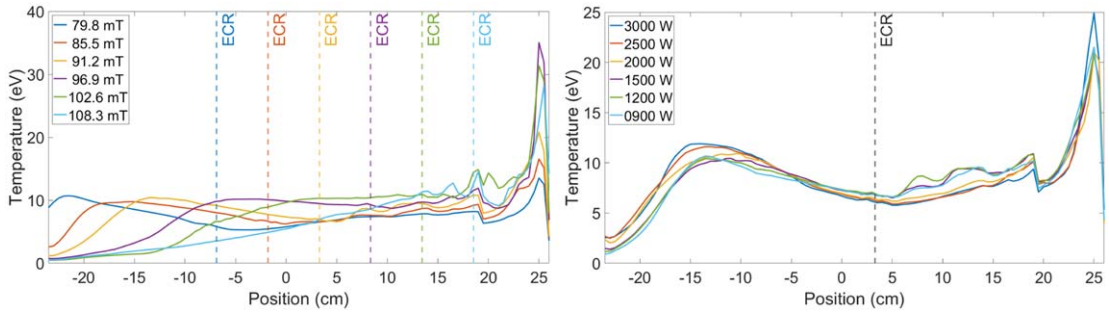

Figure 30. Influence of the magnetic field B_0 (left) and the injected power (right) on the temperature profile at $t = 1.7\ s$.

The influence of the power P_{EC} and the magnetic field B_0 on the temperature and the density are already discussed in another paper [17] in a general way. This time we will focus on the absorption mechanisms which we can identify in the temperature and density profiles in steady-state regime (figures 30 and 31) with the standard pressure of $6.35 \cdot 10^{-4}\ mbar$. We will initially consider the simplest case where the FX-wave is partly converted into an EBW at the UHR and partly tunnels through the evanescent layer.

The conversion efficiency and tunneling fraction can be evaluated by calculating the Budden parameter η which depends on the magnetic scale length L_B and the density scale length L_n evaluated at the UHR-layer [20]. This way the amount of tunneling X-wave and conversion to the EBW can be determined (figure 32). Since the magnetic scale length is nearly constant at the LFS, the conversion and tunneling efficiency depends mainly on the density scale length. Which is in this case the density slope at the LFS which is linked to the width of the evanescent layer.

The tunneling of the X-wave becomes more efficient when the size of the evanescent layer is reduced. This is clearly visible in figure 31 where the density gradient is significantly larger for the high power cases (2500 −3000 W). The calculated tunneling fraction is consequently larger (figure 32), which results in a higher density at the ECR.

The conversion efficiency to the EBW is also larger when the injected power increases. The mode converted EBW moves to the core region and EBW collisional damping occurs during propagation [25]. The collisional damping causes a density peak at ≈16.7 cm. The remaining energy is absorbed midway between the ECR and the UHR. The EBW have a large parallel refractive index $N_{\|}$ (>1), and are damped away via the Doppler-shifted cyclotron resonance [26]. In the case of $P_{EC} = 1200\ W$ and $B_0 = 92.1\ mT$ this results in a temperature peak at ≈8 cm and a density peak near ≈10 cm (figure 29) due to the convection. Similar results are observed in

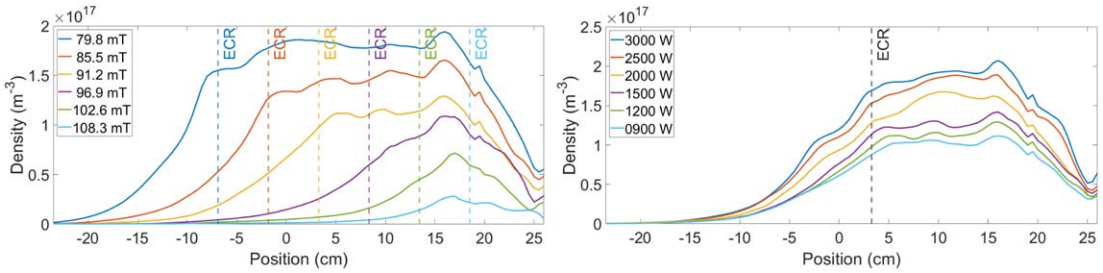

Figure 31. Influence of the magnetic field B_0 (left) and the injected power (right) on the density profile at $t = 1.7$ *s*.

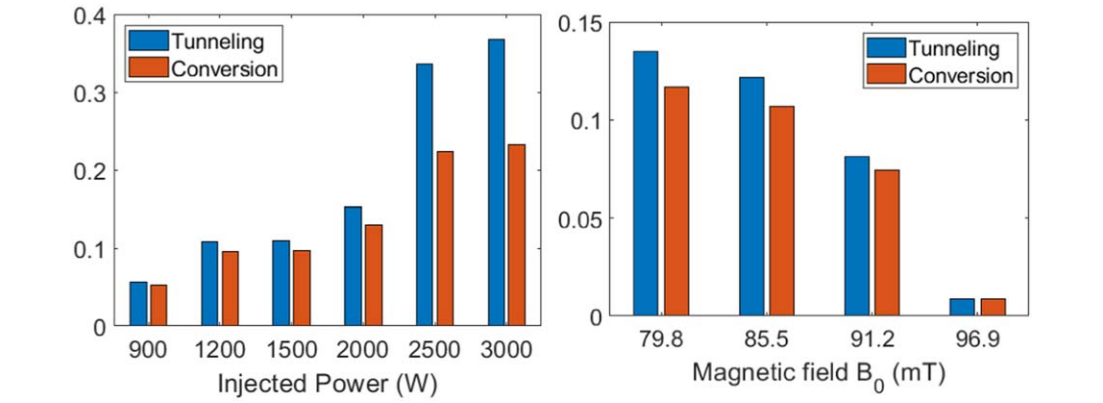

Figure 32. Tunneling and conversion fraction for various levels of the injected power P_{EC} and the magnetic field B_0.

figure 31 for higher values of the injected power—where the doppler shifted ECR moves slightly to the LFS due to the higher plasma densities.

For the highest values of the magnetic field (102.6 *mT* and 108.3 *mT*) the UHR density is not reached in the horizontal mid-plane. It is consequently hard to draw any conclusions for these scans. For decreasing values of the magnetic field we observe an increase in the conversion efficiency and the tunneling fraction. The density is consequently raised at the ECR where the tunneling X-wave is absorbed, and the doppler shifted ECR—a few cm to the LFS of the ECR—where the EBW is absorbed (figure 31). We also observe that this doppler shifted ECR moves to the LFS together with the ECR.

Additional temperature peaks are visible, especially in the cases with lower power (900 *W* − 1500 *W*), located at ≈11.7 cm, ≈13.7 cm and ≈16.7 cm. These could be the result of parametric decay at the UHR [21, 24, 27], introducing LHW or other waves into the plasma. This has to be confirmed by dedicated experiments.

It seems that the observed temperature peaks seem to vanish when the ECR is moved to the HFS (Figure 30) or the injected power is raised (figure 30). This could be linked to the fact that the density gradient becomes more steep as observed in figure 31. Consequently the width of the evanescent layer is reduced which influences strongly the tunneling of the X-wave and the conversion efficiency of the EBW, consequently reducing the fraction of the parametric instabilities.

6. Conclusion

The power deposition for Electron Cyclotron Resonance Heating in helium was studied in TOMAS. Initially we characterized the ECRH power source and determined the fraction of reflected power for several values of the injected power P_{EC}, the magnetic field B_0 and the gas pressure. They influence the plasma parameters and therefore the reflection coefficient. In most cases, about 80 to 90% of the injected power is absorbed.

The influence of the Langmuir probe position and the wave polarization was examined. We can conclude that the probe hardly influences the plasma for an X-wave polarization of the injected wave and only slightly for the O-wave.

The temperature and density profiles, obtained by the triple Langmuir probe, were used to determine the power deposition mechanisms present in the vessel. Resonant coupling at the electron cyclotron resonance layer causes plasma breakdown and the initial plasma build-up. The polarization of the injected wave is of no importance since mode scrambling results in a mixture of both polarizations.

When the density rises a new resonance layer becomes visible; the UHR. Additionally collisional damping near the UHR and resonant coupling of the EBW at the doppler shifted electron cyclotron resonance layer was observed. The temperature profile shows some additional temperature peaks suggesting parametric decay at the UHR introducing LHW or other waves in the plasma. A steep density profile at the LFS seems to reduce the fraction of decay. This can be achieved by raising the injected power or reducing the magnetic field.

The origin of the additional temperature peaks will be investigated in future experiments to verify if parametric decay at the UHR is responsible for these. The amount of stray radiation will also be assessed.

Data availability statement

The data cannot be made publicly available upon publication because they are not available in a format that is sufficiently accessible or reusable by other researchers. The data that support the findings of this study are available upon reasonable request from the authors.

References

[1] Sips A C C, Giruzzi G, Ide S, Kessel C, Luce T C, Snipes J A, Stober J K and the Integrated Operation Scenario Topical Group of the ITPA 2014 Progress in preparing scenarios for operation of the International Thermonuclear Experimental Reactor *Phys. Plasmas* **22** 021804

[2] Leuer J A and Wesley J C 1993 Iter plasma start-up modeling *15th IEEE/NPSS Symposium. Fusion Engineering* vol.2 629–33

[3] Minashin P V, Alexander Kukushkin and Khayrutdinov R R 2015 and Victor Lukash. A model of multi-pass absorption of external ec radiation at initial stage of discharge in iter *EPJ Web. of Conferences* **87** 03005

[4] Stober J *et al* the ASDEX Upgrade Team the TJ-II Team the ITPA 'Integrated Operations Scenarios' Group Members, and Experts 2011 Ecrh-assisted plasma start-up with toroidally inclined launch: multi-machine comparison and perspectives for iter *Nucl. Fusion* **51** 0830

[5] Lloyd B, Carolan P G and Warrick C D 1996 Ecrh-assisted start-up in iter *Plasma Phys. Controlled Fusion* **38** 16

[6] de Vries P C and Gribov Y 2019 Iter breakdown and plasma initiation revisited *Nucl. Fusion* **59** 096043

[7] Bae Y S *et al* 2008 Ech pre-ionization and assisted startup in the fully superconducting kstar tokamak using second harmonic *Nucl. Fusion* **49** 022001

[8] Kirit P and Pradhan S 2016 Observation on fundamental and second harmonic mode ecrh assisted plasma startup in sst-1 experiments *Fusion Eng. Des.* **106** 99–102

[9] Buermans J 2023 X-mode electron cyclotron heating scenarios beyond the cut-off density *AIP Conf. Proc.* 2984 110003

[10] Westerhof E 2012 Electron cyclotron waves *Fusion Sci. Technol.* **61** 304–11

[11] Moseev D, Laqua H, Marsen S, Stange T, Braune H, Erckmann V, Gellert F, Oosterbeek J W, Wenzel U and W7-X Team 2017 Experimental investigation of the ecrh stray radiation during the start-up phase in wendelstein 7-x *EPJ Web. Conf.* **147** 03002

[12] Gandini F 2023 Refinement of the ec stray radiation estimates for iter *EPJ Web. Conf.* **277** 01007

[13] Störk H B *et al* 2001 TOMAS—a toroidal magnetized plasma facility for studying wall conditioning of future fusion devices *Fusion Technol.* **39** 54–60

[14] Goriaev A *et al* 2021 The upgraded TOMAS device: A toroidal plasma facility for wall conditioning, plasma production, and plasma-surface interaction studies *Rev. Sci. Instrum.* **92** 023506

[15] Kovtun Y *et al* 2023 Overview of TOMAS plasma diagnostics *J. Instrum.* **18** C02034

[16] Chen S-L and Sekiguchi T 1965 Instantaneous direct-display system of plasma parameters by means of triple probe *J. Appl. Phys.* **36** 2363–75

[17] Buermans J *et al* 2023 Characterization of ECRH plasmas in TOMAS *Submitted for publication to Nuclear Fusion*

[18] Nowak S, Airoldi A, Bruschi A, Cirant S, Gandini F, Granucci G, Lazzaro E, Ramponi G, Simonetto A and Sozzi C 2001 Measurements of residual power of EC waves propagating in FTU tokamak during ECRH experiments at 140 ghz *Fusion Eng. Des.* **53** 315–20

[19] Buermans J *et al* 2023 Triple Langmuir probe calibration in TOMAS ECRH plasma *AIP Adv.* **13** 055125

[20] Budden K G 1979 Resonance tunnelling of waves in a stratified cold plasma *Philosophical Transactions of the Royal Society of London. Series A, Mathematical and Physical Sciences* **290** 405–33

[21] Lee J J H, Kim S, Kim S, An Y and Hwang Y-s 2017 Efficient pre-ionization by direct X-B mode conversion in VEST *Phys. Plasmas* **24** 012103

[22] Marshall N 1972 Rosenbluth. Parametric instabilities in inhomogeneous media *Phys. Rev. Lett.* **29** 565–7

[23] Popov A Y, Gusakov E Z and Saveliev A 2012 On the low-threshold parametric mechanism of the anomalous power absorption in electron cyclotron resonance heating experiments in toroidal devices *JETP Lett.* **96** 164–70

[24] Westerhof E *et al* 2009 Strong scattering of high power millimeter waves in tokamak plasmas with tearing modes *Phys. Rev. Lett.* **103** 125001

[25] Lee H, Hwang Y S, Jo J, Yang J, Chung K J and Kim S-H 2018 *26th IAEA Fusion Energy ConferenceStudy on EBW assisted startup and heating experiments via direct XB mode conversion from low field side injection in VEST* (London) IAEA-CN–234

[26] Maekawa T, Kobayashi T, Yamaguchi S, Yoshinaga K, Igami H, Uchida M, Tanaka H, Asakawa M and Terumichi Y 2001 Doppler-shifted cyclotron absorption of electron bernstein waves via $n_{\|}$-upshift in a tokamak plasma *Phys. Rev. Lett.* **86** 3783–6

[27] Dodin I Y and Arefiev A V 2017 Parametric decay of plasma waves near the upper-hybrid resonance *Phys. Plasmas* **24** 032119